Research Article

Nano Research
2023, 16(4): 4698–4705

ISSN 1998-0124 CN 11-5974/O4
https://doi.org/10.1007/s12274-022-5134-4

$Cu_{2+1}O/CuO_x$ heterostructures promote the electrosynthesis of C_{2+} products from CO_2

Rongbo Sun[1,§], Cong Wei[1,§], Zixiang Huang[3,§], Shuwen Niu[1], Xiao Han[1], Cai Chen[1], Haoran Wang[1], Jia Song[1], Jun-Dong Yi[1], Geng Wu[1], Dewei Rao[2] (✉), Xusheng Zheng[3], Yuen Wu[1], Gongming Wang[1] (✉), and Xun Hong[1] (✉)

[1] *Center of Advanced Nanocatalysis (CAN), Department of Applied Chemistry, University of Science and Technology of China, Hefei 230026, China*
[2] *School of Materials Science and Engineering, Jiangsu University, Zhenjiang 212013, China*
[3] *National Synchrotron Radiation Laboratory (NSRL), University of Science and Technology of China, Hefei 230026, China*
[§] *Rongbo Sun, Cong Wei, and Zixiang Huang contributed equally to this work.*

Received: 20 September 2022 / **Revised:** 29 September 2022 / **Accepted:** 1 October 2022

ABSTRACT

Manipulating the oxidation state of Cu catalysts can significantly affect the selectivity and activity of electrocatalytic carbon dioxide reduction (CO_2RR). However, the thermodynamically favorable cathodic reduction to metallic states typically leads to catalytic deactivation. Herein, a defect construction strategy is employed to prepare crystalline/amorphous $Cu_{2+1}O/CuO_x$ heterostructures (c/a-CuO_x) with abundant Cu^0 and $Cu^{\delta+}$ ($0 < \delta < 1$) sites for CO_2RR. The C_{2+} Faradaic efficiency of the heterostructured Cu catalyst is up to 81.3%, with partial current densities of 406.7 mA·cm^{-2}. Significantly, real-time monitoring of the Cu oxidation state evolution by *in-situ* Raman spectroscopy confirms the stability of $Cu^{\delta+}$ species under long-term high current density operation. Density functional theory (DFT) calculations further reveal that the adjacent Cu^0 and $Cu^{\delta+}$ sites in heterostructured c/a-CuO_x can efficiently reduce the energy barrier of CO coupling for C_{2+} products.

KEYWORDS

CO_2 electroreduction, C–C coupling, heterostructures, *in-situ* Raman, manipulation of oxidation states

1 Introduction

Electrochemical CO_2 reduction reaction (CO_2RR) for value-added carbon-based products, potentially driven by renewable energies, is a promising way to step toward a sustainable energy economy [1–3]. Catalysts are the key functional components for CO_2RR and play vital effects on the reaction kinetics and product selectivity. Recently developed CO_2RR electrocatalysts such as Au, Ag, and Pd can convert CO_2 into C_1 products such as carbon monoxide (CO), methane (CH_4), and formic acid (HCOOH), possessing high Faradaic efficiencies (FE) and selectivity at large current densities [4–6]. However, the deeper reduction of these products into more energy-intensive, higher-value C_{2+} oxygenates, and hydrocarbons is usually limited by unsatisfactory efficiencies and reaction rates [7, 8]. As the exclusive metal catalyst to form multi-carbon products via CO_2RR, Cu can produce up to 16 different products, such as ethylene (C_2H_4), ethanol (C_2H_5OH), and n-propanol (C_3H_7OH), etc [9–11]. Due to the variety of possible products, the major challenge faced by Cu is the poor selectivity toward C_{2+} products. In light of practical application, how to manipulate the catalytic surface of Cu for selective catalysis is the key to achieving efficient conversion from CO_2 to valuable products [12, 13].

To improve the selectivity of Cu, various strategies have been explored, including morphology and size manipulation, alloying, surface modification with molecules, crystal face engineering, and oxidation state regulation [14–16]. Among them, oxidized Cu-based catalysts hold great promise with tunable interfacial properties and local chemical environments [17, 18]. It has been found that the $Cu^{\delta+}$ species under CO_2RR conditions correlate closely with the generation of C_{2+} products [19, 20]. For instance, Kanan and co-workers have shown that the preoxidation of Cu can retain active Cu^+ species, which significantly boosts its intrinsic catalytic properties toward C_{2+} formation. Chen group put forward the correlation between the oxidation state of Cu sites and their individual selectivity toward CO_2RR (mixed Cu^+ and Cu^0, Cu^+-dominated, and Cu^0-dominated corresponding to C_2H_4/C_2H_5OH, CO/$HCOO^-$, and CH_4, respectively). Moreover, *in-situ* studies further revealed that the oxidized Cu^+ species in the catalysts generally undergo time-dependent variation and finally reach a dynamically stable state as the CO_2RR proceeds [21, 22]. However, $Cu^{\delta+}$ species are thermodynamically inclined to be reduced to Cu^0 at the CO_2 reduction potential region, intrinsically limiting the continuous and efficient generation of C_{2+} products [23]. In this regard, constructing stable $Cu^{\delta+}$ active sites which can tolerate large current operations toward CO_2RR is an urgent issue that needs to be overcome [24].

Herein by a defect construction approach, we prepared stable and atypical oxygen-containing copper heterostructures ($Cu_{2+1}O/CuO_x$). The obtained catalyst exhibits outstanding CO_2RR performance with over 80% Faradaic efficiency of the C_{2+} products, outperforming most of copper oxide electrodes reported in the Refs. [25–34]. Using *in-situ* Raman spectroscopy, we tracked the $Cu^{\delta+}$ species maintaining stability under CO_2 reduction

Address correspondence to Xun Hong, hongxun@ustc.edu.cn; Gongming Wang, wanggm@ustc.edu.cn; Dewei Rao, dewei@ujs.edu.cn

conditions. More importantly, the density functional theory (DFT) calculations demonstrate that adjacent Cu^0 and $Cu^{\delta+}$ working as the heterogeneous active sites enable a synergic role in improving the selectivity of C_{2+} products.

2 Experimental section

2.1 Chemicals

All materials were obtained from commercial suppliers and used without further purification. Copper(II) 2,4-pentanedionate ($Cu(acac)_2$, 98%) was purchased from Sinopharm Chemical Reagent Co., Ltd (Ourchem). Sodium nitrate ($NaNO_3$, ≥ 99.0%) was purchased from Sinopharm Chemical Reagent Co., Ltd (Shanghai, China). EtOH was purchased from Sinopharm Chemical Reagent Co., Ltd (Shanghai, China). Deionized (DI) water from Milli-Q System (Millipore, Billerica, MA) was used in all our experiments.

2.2 Synthesis of amorphous CuO_x (a-CuO_x) nanosheets and crystalline/amorphous $Cu_{2+1}O/CuO_x$ (c/a-CuO_x) heterostructures

The synthesis of a-CuO_x nanosheets and c/a-CuO_x heterostructures with different crystal structures was prepared by adjusting the calcination time. In a typical synthesis, a certain amount of the metal organic compound ($Cu(acac)_2$, 5 mg) and the inorganic salt ($NaNO_3$, 17 mg) were dispersed in the ethanol solution, the resulting mixture was sonicated until a uniformly stable mixed solution was formed. Then, the mixture was poured into an open container, after the solvent was evaporated at 70 °C, the obtained solid powder was taken out and grounded in an agate mortar for 5 to 10 min, then the as-prepared solid was transferred to a porcelain boat and heated at a temperature of 533.15 K in a tube furnace under an argon atmosphere flow (120 sccm) for 1 or 2 h. After naturally cooled to room temperature, the resulting products were collected by centrifugation and washed three times with deionized water. At extended calcination time, crystalline $Cu_{2+1}O$ nanoparticles with a stable crystal structure were formed.

2.3 Characterization

Powder X-ray diffraction (XRD) patterns of samples were recorded on a Rigaku Miniflex-600 operating at 40 kV voltage and 15 mA current with Cu Kα radiation (λ = 0.15406 nm). X-ray photoelectron spectroscopy (XPS) was collected on scanning X-ray microprobe (PHI 5000 Verasa, ULAC-PHI, Inc.) by Al Kα radiation and the C 1s peak located at 284.8 eV as standard. Transmission electron microscopy (TEM) was carried out by a Hitachi-7700 working at 100 kV. The high-resolution TEM (HRTEM), high-angle annular dark-field scanning TEM (HAADF-STEM), and electron energy loss spectrometry (EELS) mapping were recorded by JEOL JEM-ARM200F TEM/STEM with a spherical aberration corrector working at 200 kV.

2.4 Preparation of gas diffusion electrodes (GDEs)

Carbon paper (Sigracet 35 BC) with a microporous layer (MPL) was purchased from the fuel cell store. 5 mg of catalyst was mixed with 40 μL of 5 wt.% Nafion solution and 5 mL ethanol solvent. The solution was sonicated for at least 60 min at room temperature and stirred for at least 6 h to form a homogeneous ink. The well-dispersed ink was then airbrushed onto a gas diffusion layer (2.5 cm × 2.0 cm) using an Anest Iwata RG-3L airbrush (Japan) pumped by an air compressor at a fixed pressure of 60 p.s.i. The GDEs were cut to 2.5 cm × 1.0 cm and dried in a vacuum chamber overnight before use. The loading amount was determined by weighing the GDEs before and after the airbrushing, and was found to be roughly 1.0 mg·cm^{-2}.

2.5 Electrochemical measurement

The gas-tight flow cell system was fabricated with a CO_2 gas compartment and two liquid compartments with channels of dimensions 2.0 cm × 0.5 cm × 0.3 cm (Fig. S13 in the Electronic Supplementary Material (ESM)). All electrochemical measurements were performed in a flow cell with a VSP-300 potentiostat (Bio-Logic, France). The electrolyte (1 M KOH) was circulated through both the anode (nickel foam) and cathode chambers separated by the anion exchange membrane (AEM, Fumasep FAB-3-PK-130). The CO_2 (99.999%) and KOH electrolyte flow were kept constant at 24 and 20 mL·min^{-1} controlled by a mass flow controller (C100L, Sierra) and a peristaltic pump (BT100-2J, Longer Pump), respectively. The applied potentials were measured against a Ag/AgCl reference electrode in saturated KCl and converted to the reversible hydrogen electrode (RHE) reference scale with *iR* correction by

$$E(\text{vs. RHE}) = E(\text{vs. Ag/AgCl}) + 0.205 + (0.0591 \times \text{pH}) - iR_s \quad (1)$$

where the solution resistance R_s was determined by electrochemical impedance spectroscopy at frequencies ranging from 0.1 to 100 kHz.

2.6 CO_2RR product analysis

To accurately quantify the gas products during CO_2 electrolysis, the gas outlet flow rate from the reactor was carefully monitored by a mass flow meter (AST10-HLC, Asert Instruments) at each current density. The gas chromatograph (GC-2014, Shimadzu) analysis was set up to split the gas sample into two aliquots. One aliquot passed a thermal conductivity detector to quantify H_2 concentration, and the other was routed through a flame ionization detector with a methanizer to quantitatively analyze the content of CO and alkane species. The Faradaic efficiency for gas products was calculated by the following formula

$$\text{FE}(\%) = 100 \times \frac{nxFV}{j_{\text{total}}} \quad (2)$$

where n and x are the number of electrons transferred and the mole fraction of a certain product, respectively, F is Faradaic constant, V is the total molar flow rate of gas, and j_{total} is the measured total current.

^{1}H nuclear magnetic resonance (^{1}H NMR) spectra measured with water suppression using a presaturation method were collected on a Bruker 400 MHz spectrometer to test liquid products. Typically, 500 μL of electrolyte after CO_2RR electrolysis was mixed with 100 μL of D_2O containing 50 ppm (m/m) dimethyl sulfoxide as the internal standard. The same spectral acquisition parameters were used for all measurements to ensure complete relaxation and quantification. The presented data were the accumulated result of 32 scans.

3 Results and discussion

Figure 1(a) schematically shows the formation process of c/a-CuO_x. Firstly, the a-CuO_x nanosheets were prepared by annealing the mixture of $Cu(acac)_2$ and $NaNO_3$ in Ar at 260 °C for 1 h, and the structural characterizations were shown in Fig. S1 in the ESM [35]. Subsequently, the calcination time was extended to 2 h to form crystalline $Cu_{2+1}O$ (Cu_2O with oxygen vacancies) nanoparticles. The *in-situ* reduction mechanism was confirmed by the thermal gravimetric analyzer coupled with mass spectrometry (TGA-MS, Fig. S2 in the ESM). The production of CO was

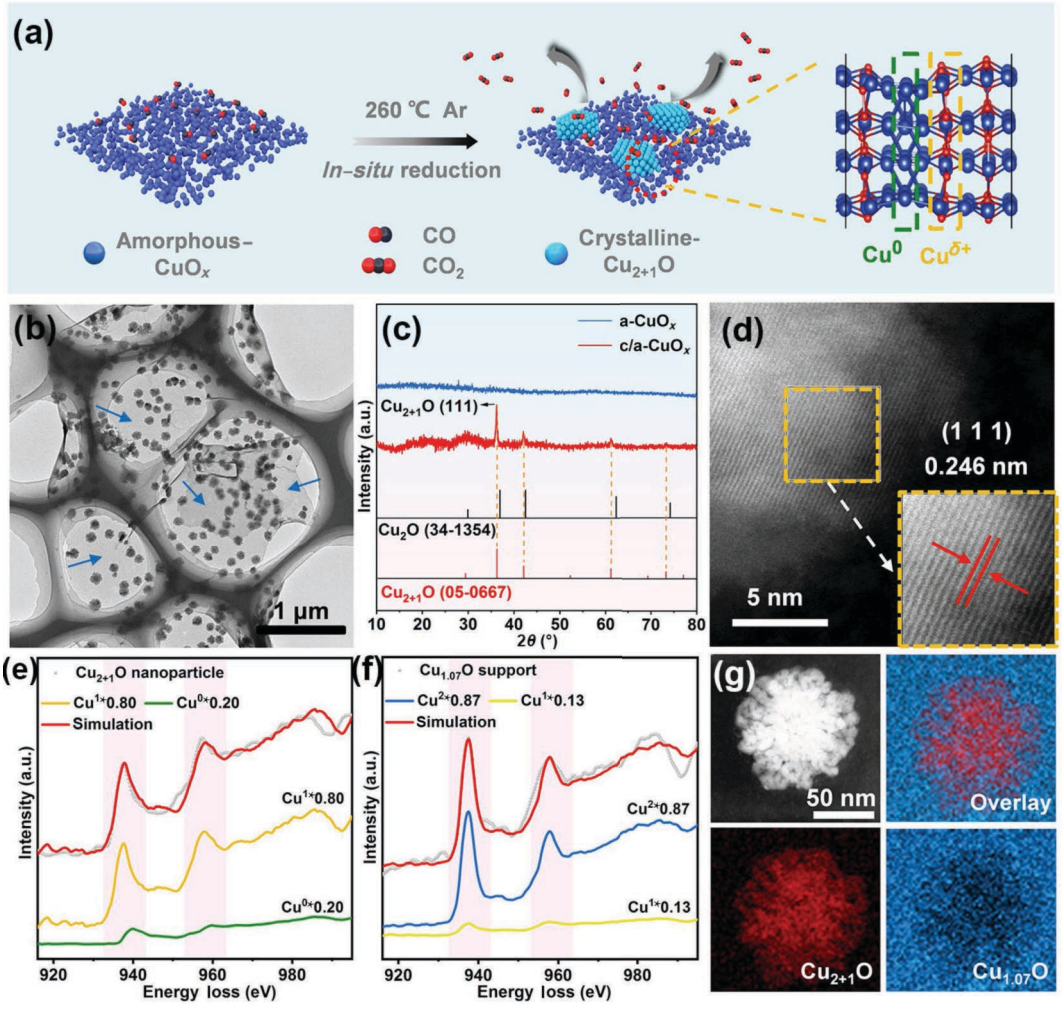

Figure 1 Schematic illustrations and structural characterizations. (a) Schematic preparation process and enlarged diagram of the atomic structure. (b) TEM image of c/a-CuO_x, the blue marks the amorphous CuO_x. (c) XRD patterns of a-CuO_x and c/a-CuO_x. (d) Atomic resolution HAADF-STEM images of $Cu_{2+1}O$. The normalized EELS of Cu from (e) the $Cu_{2+1}O$ nanoparticles and (f) a-CuO_x nanosheets. (g) HAADF-image, the valence states distribution of Cu in a typical c/a-CuO_x, in which $Cu_{2+1}O$ and $Cu_{1.07}O$ are indicated in red and blue, respectively.

detected during the heating process, which is the key agent for reducing a-CuO_x to $Cu_{2+1}O$. Furthermore, TEM images (Fig. 1(b) and Fig. S3 in the ESM) revealed the $Cu_{2+1}O$ nanoparticles are supported on amorphous nanosheets with lateral dimensions up to micron level. The elemental mapping images (Fig. S4 in the ESM) display the uniform dispersion of Cu, O, and C. In the XRD patterns shown in Fig. 1(c), the peak at 36.418° can be indexed well to the $Cu_{2+1}O$ (111) diffraction (JCPDS 05-0667). Compared with the standard Cu_2O (JCPDS 34-1354), a shift of ~ 0.6° was observed on $Cu_{2+1}O$, suggesting the formation of oxygen vacancies during the reduction process.

The fine structure of c/a-CuO_x was further clarified by the atomic resolution HAADF-STEM and HRTEM images (Fig. 1(d) and Figs. S5 and S6 in the ESM). The diameter of $Cu_{2+1}O$ nanoparticles is about 100 nm, and the amorphous/crystalline interface can be observed. It can be recognized from the magnified HAADF-STEM images in Fig. 1(d) and Fig. S6 in the ESM that the crystalline area appears a lattice spacing of 0.246 nm, which could be indexed to the (111) plane of the $Cu_{2+1}O$ with a space group of $Pn\bar{3}m$. Moreover, fine-structure analyses of the EELS spectra were applied to determine the valence of c/a-CuO_x (Figs. 1(e)–1(g) and Fig. S7 in the ESM). The valence-state distribution of Cu was mapped by processing the "white lines" in the EELS spectra [36, 37]. The normalized EELS spectra of Cu from the nanoparticle and support are shown in Figs. 1(e) and 1(f). The EELS spectrum from the nanoparticle shows a lower L_3 intensity than that of the support, indicating different valence states in the two parts. The valence-state distribution of Cu was extracted by utilizing a multiple linear least-squares fitting method. As shown in Fig. 1(g), $Cu_{2+1}O$ (red) and $Cu_{1.07}O$ (blue) were distributed in the nanoparticle and support, respectively. The results confirm that the valence states of Cu in the crystalline and amorphous parts of the c/a-CuO_x heterostructures are close to those of $Cu_{2+1}^{(+0.7)}O$ and $Cu^{(+2)}O$, respectively (see Notes S1 and S2 in the ESM for a detailed discussion).

The XPS survey of a-CuO_x and c/a-CuO_x confirmed that Cu, C, and O elements exist in the material (Fig. S8 in the ESM). In the core-level XPS Cu 2p spectra shown in Fig. 2(a), the binding energies centered at 932.4 and 952.3 eV are stemmed from the spin orbital component $2p_{3/2}$ and $2p_{1/2}$ of Cu(0)/Cu(I), while the peaks at 936.8 and 957.0 eV are attributed to the characteristics of Cu(II) [38]. The as-prepared c/a-CuO_x exhibits distinct Cu(0)/Cu(I) valence state features, confirming the reduced Cu valence. To further distinguish the Cu(0)/Cu(I), Auger spectroscopy was performed. The Cu $L_3M_{45}M_{45}$ Auger spectra show that Cu(0)/Cu(I) species coexisted on the surface of c/a-CuO_x. In contrast, only a weak Cu(0) signal can be observed in a-CuO_x, indicating that a-CuO_x was reduced during the annealing process (Fig. 2(b)) [39]. The oxygen vacancies induced by the thermal reduction were further probed by the XPS O 1s spectra, which can be deconvoluted into three subpeaks (Fig. 2(c)). Specifically, the O1 peak with the binding energy around 531.8 eV

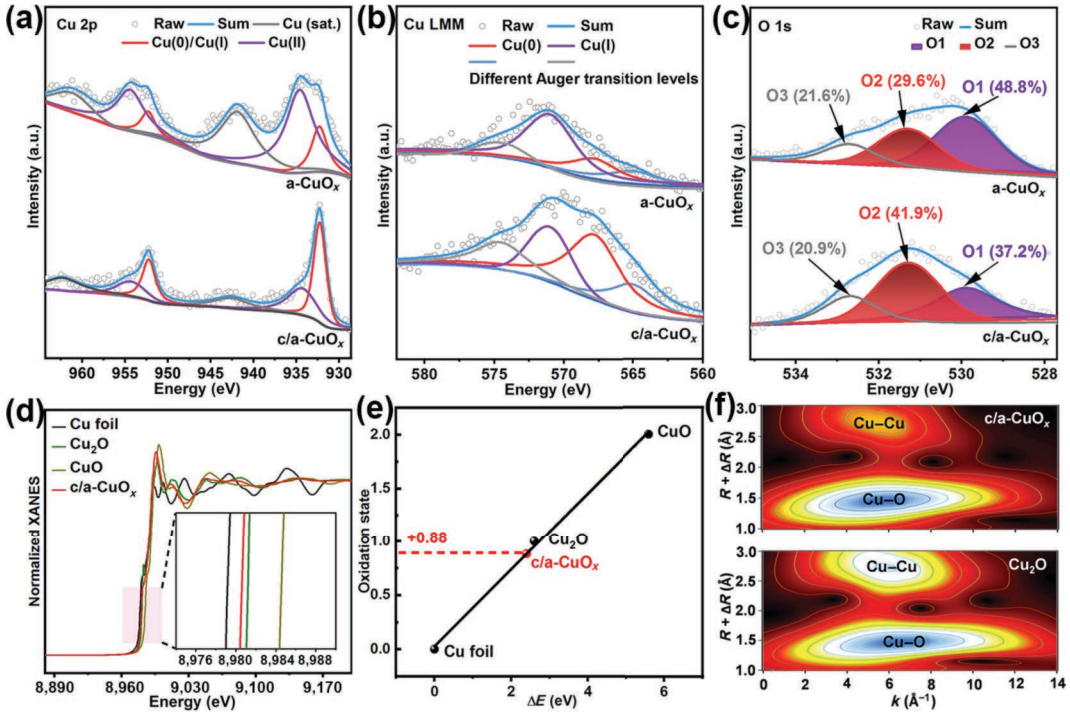

Figure 2 Structure and composition characterization of a-CuO_x and c/a-CuO_x. (a) XPS of Cu 2p spectra. (b) Cu LMM Auger spectra. (c) XPS of O 1s spectra. (d) Cu K-edge XANES spectra for Cu foil, Cu_2O, CuO, and c/a-CuO_x. (e) The calculation of Cu oxidation states from Cu K-edge XANES. (f) The wavelet transform of Cu K-edge EXAFS data for c/a-CuO_x and Cu_2O standard sample.

is attributed to the metal–oxygen bonds. The O2 peak around 533.2 eV corresponds to the defect sites with lower oxygen coordination, while the O3 peak at 534.3 eV is assigned to the hydroxyl species of the surface-adsorbed water molecules [40]. The O 1s XPS spectrum of c/a-CuO_x features a higher proportion of O2 peak, indicating rich surface oxygen vacancies. Besides, the Cu L_3-edge X-ray absorption near-edge structure (XANES) spectra shown in Fig. S9 in the ESM also consistently support the Cu(0) rich feature in c/a-CuO_x [41].

Furthermore, the X-ray absorption fine structure (XAFS) measurements were performed to reveal the electronic and coordination environment information of the c/a-CuO_x heterostructures. As shown in Fig. 2(d), the pre-edge energy of Cu in the c/a-CuO_x is located between Cu foil (0) and Cu_2O (+1), suggesting the moderate oxidation state. Since the Cu K-edge energies are linearly correlated to the oxidation states (δ) of Cu, the fitted δ value of Cu in c/a-CuO_x is estimated to be +0.88 (Fig. 2(e)) [42]. Figure S10 in the ESM shows the Fourier transformed extended XAFS (EXAFS) spectra of Cu K-edge of c/a-CuO_x and standard sample. The first nearest neighbor coordination shell of c/a-CuO_x is similar to Cu_2O, and the second coordination peak at 2.7–3.2 Å is assigned to the mixed state of Cu_2O and CuO. Linear component fitting (LCF) was carried out for the material to further study its component composition (Fig. S11 in the ESM). The Cu–Cu coordination in c/a-CuO_x was distinguished into two paths, which were respectively designated as Cu_2O (crystalline parts) and CuO (amorphous parts). The fitting results in Table S1 in the ESM showed that the content of Cu_2O was 51.9%, and the content of CuO was 48.1%. And the fitted coordination number and bond length information are summarized in Table S2 in the ESM. Additionally, the Cu–Cu coordination number in $Cu_{2+1}O$ (9.6) is slightly lower than that of standard Cu_2O (11.7), due to the existence of abundant oxygen vacancies. Moreover, the wavelet spectrum of c/a-CuO_x contains two obvious intensities of Cu–O and Cu–Cu coordination, which is in line with the corresponding curve-fitting results (Fig. 2(f)). The clear difference in Cu–Cu bond strength further confirms the change in corresponding coordination number. From the Cu K-edge $k^3\chi$(k) oscillation curves, the oscillation feature of c/a-CuO_x is very close to that of Cu_2O powder (Fig. S12 in the ESM), indicating a similar atomic configuration for the Cu site in both c/a-CuO_x and Cu_2O.

The catalytic performances of the as-prepared c/a-CuO_x for CO_2RR were carried out in 1 M KOH solution using a gastight flow-cell configuration (Fig. S13 in the ESM, see Experimental section for details). All the potentials mentioned in this work are recalibrated to the reversible hydrogen electrode. As shown in Fig. 3(a), the c/a-CuO_x exhibited higher current densities and more positive onset potentials than the a-CuO_x electrodes. To further analyze the catalytic product and the corresponding Faradaic efficiencies of all the products, both the catholyte and the anolyte were collected for ^{1}H NMR analysis (Fig. S14 in the ESM), and the outlet gas flow rate for each measurement was tracked for gas product analysis (Fig. S15 in the ESM). As shown in Fig. 3(b), representative product results were detected, including those for C_3H_7OH, acetic acid (CH_3COOH), C_2H_5OH, C_2H_4, HCOOH, CH_4, CO, and H_2. Notably, the C_2H_4 production selectivity of c/a-CuO_x underwent rapid growth with increasing applied potential, maintained at high levels over a range of applied potentials between −1.5 and −1.7 V. At the same time, the yield of HCOOH decreased with the proportion of C_{2+} products increased rapidly. Furthermore, the partial current density of C_{2+} products ($j_{C_{2+}}$) at −1.7 V was as high as 406.7 mA·cm^{-2} (Fig. 3(c)), which outperformed most of the reported copper-based electrodes. This result indicates that the c/a-CuO_x electrode holds promise to operate at industrial electrolyzer-relevant current densities. Further electrochemical tests were performed in galvanostatic mode (Fig. S16 in the ESM). As shown in Figs. 3(d) and 3(e), the maximum Faradaic efficiency of C_{2+} products was up to 81.3%, and the selectivity was maintained at ~ 80% over a wide test range of 500–700 mA·cm^{-2}. We also compared the CO_2RR performance with those previously reported catalysts in terms of C_{2+} (ball symbol) or C_2H_4 (square symbol) current densities and Faradaic efficiencies. The results obtained on the c/a-CuO_x electrode represent the best performance reported to date compared to other copper oxide electrodes (Table S3 in the ESM and Fig. 3(f)).

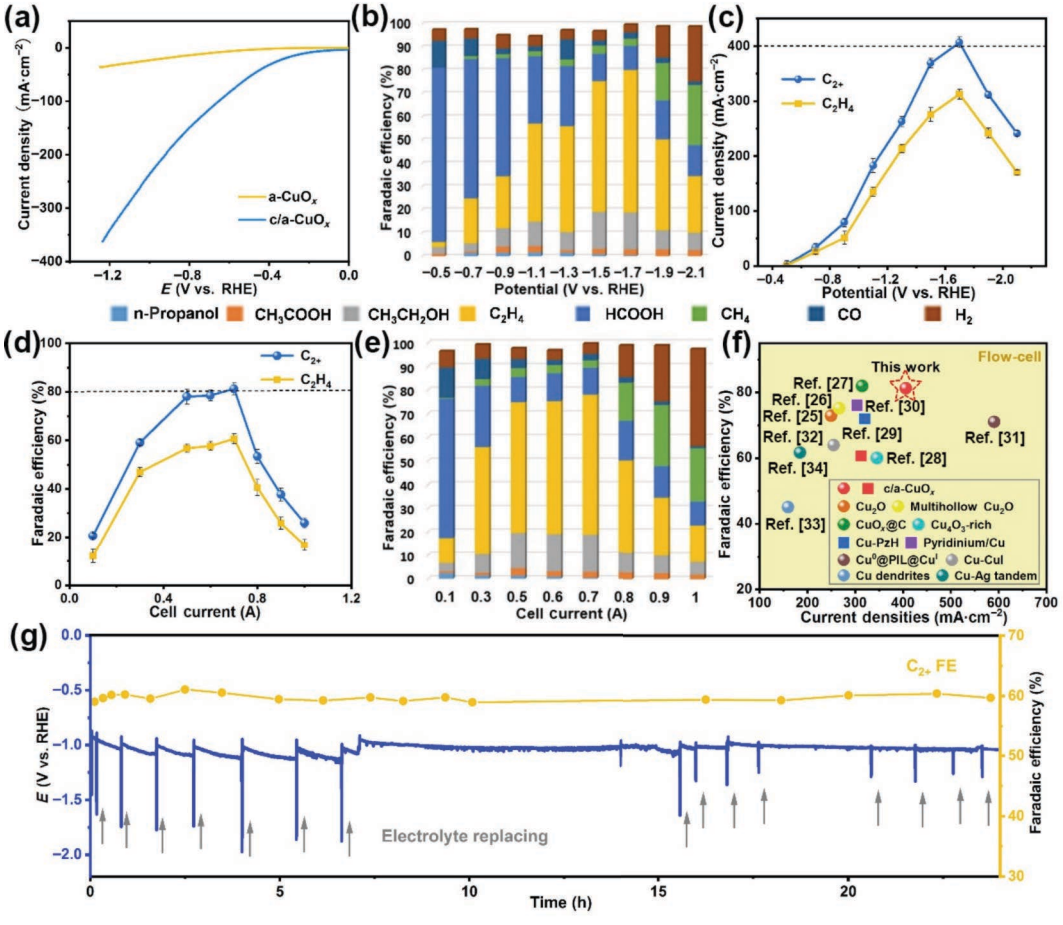

Figure 3 CO_2RR performance in a flow cell. (a) Linear sweep voltammetry curves on a-CuO_x and c/a-CuO_x electrodes. (b) Faradaic efficiencies for CO_2RR products at different potentials for c/a-CuO_x electrodes. (c) C_{2+} and C_2H_4 partial current density on c/a-CuO_x electrodes versus applied potentials. (d) C_{2+} and C_2H_4 Faradaic efficiencies on c/a-CuO_x electrodes versus different cell currents. (e) Faradaic efficiencies on c/a-CuO_x electrodes at different cell currents. (f) Comparison of C_{2+} (ball symbol) or C_2H_4 (square symbol) current densities and Faradaic efficiencies (see Table S3 in the ESM for details) for various copper-based electrodes reported in the literature. (g) Stability test of the c/a-CuO_x electrodes at a total current density of 300 mA·cm^{-2}. The electrolyte was occasionally replaced by new 1 M KOH solution (gray arrows) to recover the conductivity of the electrolyte and to avoid the possible salt accumulation. All measurements were performed in CO_2-flowed 1 M KOH electrolyte, and the reported potentials were converted to the RHE reference scale with *iR* correction. Error bars are based on the standard deviation of three independent measurements.

Long-term durability is another critical factor for assessing the practicability of catalysts. As shown in Fig. 3(g), after 24 h stability test under a constant current density of 300 mA·cm^{-2}, the ratio of C_{2+} products Faradaic efficiency was consistently maintained at ~ 60%. The electrode was found to be very stable under harsh conditions, with only a slight increase in overpotential. By replacing the electrolyte occasionally, the overpotentials and Faradaic efficiency could be maintained over 24 h long electrolysis. Meanwhile, post-mortem characterizations uncover that the material structure and oxidation state are well maintained (Figs. S17–S19 in the ESM). As shown in Figs. S20 and S21 in the ESM, the peaks remained in the XRD and *ex-situ* Raman of the c/a-CuO_x electrode after the CO_2RR measurement, indicating that the $Cu_{2+1}O$ was preserved in the testing system.

To determine whether $Cu_{2+1}O$ remained stable during the electrocatalysis CO_2RR process, *in-situ* Raman spectroscopy was applied at −1.7 V for over 30 min to investigate the structural evolution of c/a-CuO_x (Fig. S22 in the ESM). We chose the excitation wavelength of 785 nm because it can yield significant Raman intensity of related vibration modes [43]. As shown in Fig. 4(a), the peak at lower wavenumbers (450–640 cm^{-1}) is typical of Cu–O bonds. Meanwhile, several characteristic Raman peaks emerge, which arise from the Cu–CO (~ 360 cm^{-1}), CO_3^{2-} (~ 1,070 cm^{-1}), CO_2^- (~ 1,310 cm^{-1}), and carbon (~ 1,375 and ~ 1,580 cm^{-1}) modes, respectively [44]. The c/a-CuO_x electrodes exhibit Raman peaks at 525 and 621 cm^{-1}, which are attributed to the Γ^+_{25} and Γ^-_{12} + Γ^+_{25} phonon modes of Cu_2O (Fig. 4(b)) [45]. The c/a-CuO_x retains the characteristic Γ^-_{12} + Γ^+_{25} modes after 30 min, suggesting that the as-prepared catalysts effectively resist structural failure under a long-term electrochemical reduction process. Moreover, the XPS analyses of the c/a-CuO_x after electrocatalysis show that the Cu^+ species were observed after reacting for 24 h, which matches well with the Raman measurement results (Fig. S23 in the ESM).

Furthermore, we performed *in-situ* Raman spectroscopy at various applied potentials to monitor the adsorbed CO_2 reduction intermediates. The adsorbed CO (CO*) intermediates stretching frequency is sensitive not only to the type of metal but also to its charge state [46]. As shown in Figs. 4(c) and 4(d), two Raman peaks arise from the c/a-CuO_x electrode with increasing applied potential, where the peak at ~ 2,070 cm^{-1} corresponds to the stretching vibration mode of the absorbed CO* on $Cu^{\delta+}$, and the peak at ~ 2,050 cm^{-1} comes from the absorbed CO* on Cu^0 [47, 48]. The reduction of Raman signals at higher applied potential indicates that the aforementioned intermediates react at the fast CO_2 reduction kinetics. The above spectroscopic evidence has revealed that the CO* intermediate is further transformed into the C_{2+} products on the c/a-CuO_x, which is in complete agreement with the electrocatalytic performance. Combined with the above experimental evidence, we speculate on the possible mechanism of

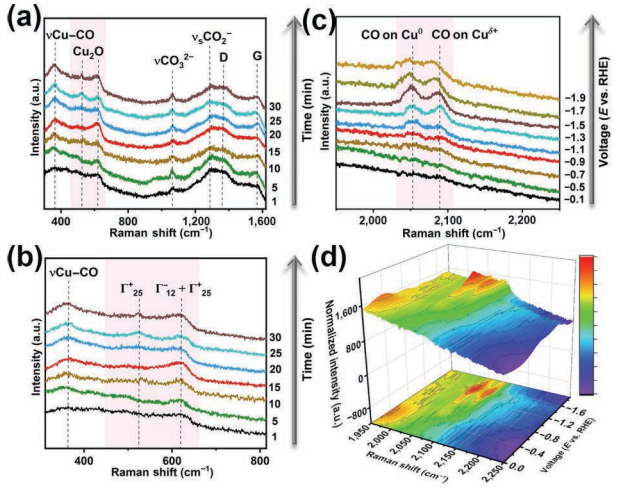

Figure 4 *In-situ* Raman studies. (a) and (b) *In-situ* Raman spectra of c/a-CuO_x as a function of reaction time at −1.7 V vs. RHE. (c) *In-situ* Raman spectra of c/a-CuO_x at the indicated potentials. (d) The corresponding three-dimensional (3D) plots of the Raman spectra and two-dimensional (2D) plots contour maps of (c). A near-infrared laser (785 nm) was used as the excitation source. All the spectra were collected after sufficient electrolysis time. Each spectrum was the representative of multiple measurements at different time scale of electrolysis. CO_2 was continuously flowed to the electrolyte during measurement.

stable existence of Cu^+ species: The c/a-CuO_x surface contains abundant Cu^0 and $Cu^{\delta+}$ ($0 < \delta < 1$) sites, which provide a suitable adsorption environment for CO* intermediates. The high local concentration of carbon intermediates could mask the active CO_2RR surface thereby stabilizing $Cu^{\delta+}$ species [24, 26].

To reveal the essences of chemical states of Cu active sites toward C_{2+} selectivity at the atomic level, theoretical calculations were performed. A simplified model of partially reduced Cu_2O (111) surface as $Cu_{2+1}O$ was constructed, based on the fine structure characterization (Fig. S24 in the ESM). As illustrated in Fig. 5(a) and Fig. S25 in the ESM, the Bader charge demonstrates the presence of Cu^0 and $Cu^{\delta+}$ on the $Cu_{2+1}O$ surface (see ESM for the detailed modeling procedure). In addition, Cu (111) and Cu_2O (111) were taken as models for the presence of Cu^0 and $Cu^{\delta+}$ individually, respectively. The stability of $Cu_{2+1}O$ was firstly explored. It is well known that, the effect of reaction conditions such as temperature or solvent on the structure of $Cu_{2+1}O$ cannot be simulated by static DFT calculations. Therefore, *ab initio* molecular dynamics (AIMD) simulations were performed. First, AIMD simulations were performed for $Cu_{2+1}O$ at the synthesis temperature (260 °C) for a lasting 30 ps, and the structure was confirmed to be stable by analyzing the root-mean-square displacement of $Cu_{2+1}O$ (111) over the simulation time (Fig. S26(a) in the ESM). In addition, AIMD simulations under reaction conditions were further considered by adsorbing solvent water on the surface, and it was found that the surface structure changed very little during the 30 ps simulation, indicating that the structure is stable under these conditions (Fig. S26(b) in the ESM).

The adsorbed CO intermediates have been identified as a critical link between CO_2 and other reduction products [49]. Like a consequence, the CO formation via CO_2 reduction over Cu (111), Cu_2O (111), and $Cu_{2+1}O$ was simulated. Figures S27–S29 in the ESM show the calculated free energy profiles for the activation of CO_2 to form CO or HCOOH at U = 0 V. Clearly, $Cu_{2+1}O$ optimizes the kinetics and thermochemistry of CO_2 activation to generate CO compared to Cu metal or Cu_2O catalysts. This $Cu_{2+1}O$ catalyst provides two essentially different active positions, helping to stabilize the negative charge on the chemisorbed CO_2 (CO_2-chem). Notably, although the order of CO generation is $Cu_{2+1}O$ (111) > Cu (111) > Cu_2O (111), respectively, where Cu_2O is more inclined to form HCOOH, $Cu_{2+1}O$ (111) and Cu (111) generate CO at particularly low overpotentials, which is consistent with previous results [50, 51].

Since the surface adsorption behavior of the catalyst is closely related to the electronic coupling between the 3d orbital of the Cu catalyst and the 5σ orbital of the CO, the density of states were further analyzed. According to the Blyholder model [52], as displayed in Fig. 5(b), the project density of states (PDOS) shows that the decrease in σ orbitals energy and the increase in π* orbitals energy resulting from the interaction of CO with the $Cu^{\delta+}$ site in $Cu_{2+1}O$ are substantially better than the CO on Cu^0 site of $Cu_{2+1}O$. Furthermore, the crystal orbital Hamilton population (COHP) analysis indicates that the interaction of CO with the $Cu^{\delta+}$ site in $Cu_{2+1}O$ produces significantly fewer antibonding states below the Fermi level than the interaction of Cu^0 with CO, implying that $Cu^{\delta+}$ exhibits stronger CO adsorption than Cu^0 (as shown in the purple dashed box and the corresponding enlarged part of Fig. 5(b)). In addition, the ICOHP values verify that the Cu–C (2.96 eF) and C–O (10.90 eF) bonds on $Cu^{\delta+}$ are stronger

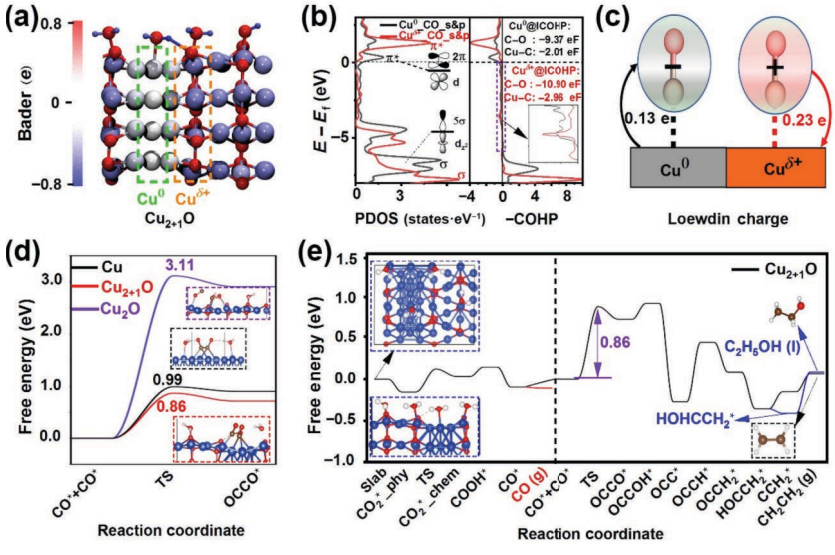

Figure 5 DFT calculations. (a) Bader charge of $Cu_{2+1}O$ surface. (b) PDOS and COHP of CO adsorbed on the $Cu_{2+1}O$ surface's Cu^0 and $Cu^{\delta+}$ sites. (c) Loewdin charge. (d) The C–C coupling step for Cu, $Cu_{2+1}O$, and $Cu_{2+1}O$. (e) Dominant path and associated reaction energetics identified for ethylene and ethanol production starting with CO_2 on the $Cu_{2+1}O$ surface at 0 V vs. RHE. Energy values are referenced to the CO_2 (g), H^+ (aq) + e^- pair and a $Cu_{2+1}O$ surface. Color code: Cu, blue; O, red; C, gray; H, white.

than those on Cu^0 of Cu–C (2.01 eF) and C–O (9.37 eF) bonds. Also, charge analysis (including Bader, Loewdin, and Mulliken) indicates that CO adsorbed at the Cu^0 site causes the Cu surface to feedback electrons to CO. In contrast, CO adsorbed at the $Cu^{\delta+}$ site is positively charged due to electron loss (Fig. 5(c) and Table S4 in the ESM). Naturally, for the activation free energy of CO* coupling to generate OCCO*, the $Cu_{2+1}O$ (0.86 eV) shows an even better improvement than the Cu (111) (0.99 eV) and Cu_2O (111) (3.11 eV) surfaces (Fig. 5(d)). This is because that the $Cu_{2+1}O$ provides two different adsorption environments for CO*. The difference in CO* positive and negative charges narrows the distance of CO* coupling (Fig. S30 in the ESM illustrates the corresponding structural information) by electrostatic attraction and thus reduces the energy barrier of CO* coupling.

Based on the above structural information, we further elucidated the reaction pathway for the conversion of CO_2 to C_2 product ethylene. As shown in Fig. 5(e) (left of dashed line), starting with CO_2, the optimal path for forming CO* in $Cu_{2+1}O$ is CO_2*_phy → CO_2*_chem → COOH → CO, where CO_2 activation is the rate-determining step (RDS) that results in CO*, and the activation free energy to overcome is 0.27 eV. Furthermore, as shown on the right side of the dashed line in Fig. 5(e) and Fig. S31 in the ESM, the production of ethylene from CO + CO is mainly via CO + CO → OCCO → OCCOH → OCC → OCCH → $OCCH_2$→ $HOCCH_2$ → CCH_2 → C_2H_4 (g), where the CO coupling determines the C_2 production efficiency, which is consistent with our *in-situ* Raman results. Since CH_2COH has been regarded as an essential intermediate in forming the C_2 product of ethanol or ethylene [1, 2], our calculations also indicate that $Cu_{2+1}O$ prefers to produce ethylene via the CH_2C intermediate rather than ethanol via the CH_2CHOH intermediate.

4 Conclusions

In conclusion, we have demonstrated a structural design methodology for fabricating CO_2RR electrocatalysts with high selectivity and stability. The as-prepared crystalline/amorphous $Cu_{2+1}O/CuO_x$ heterostructure catalyst possesses abundant $Cu^{\delta+}$ sites, thus delivering sufficient active sites for the stabilization and enrichment of critical intermediates. The c/a-CuO_x exhibits high C_{2+} selectivity, excellent Faradaic efficiency, high current density, and long-term cyclic stability in CO_2RR. Furthermore, *in-situ* Raman spectroscopy confirms the catalytic stability of $Cu^{\delta+}$ at large CO_2RR current densities. Theoretical investigation reveals that the synergic roles of adjacent heterogeneous active sites narrow the distance of CO* coupling, crucially improving the catalytic selectivity. This work could provide new guidance for designing high-performance Cu-based catalysts for CO_2RR.

Acknowledgements

This work was supported by the National Key R&D Program of China (Nos. 2017YFA0700104 and 2018YFA0702001), the National Natural Science Foundation of China (Nos. 21871238 and 22175163), the Fundamental Research Funds for the Central Universities (No. WK2060000016), and the Youth Innovation Promotion Association of the Chinese Academy of Science (No. 2018494). We thank the photoemission end stations (BL10B) in National Synchrotron Radiation Laboratory (NSRL) and BL14W1 in Shanghai Synchrotron Radiation Facility (SSRF) for help in characterizations.

Electronic Supplementary Material: Supplementary material (the detailed TEM and SEM images, HAADF-STEM images, EDX spectra, TGA-MS data, EELS spectra, XPS data, XANES spectra, EXAFS fitting spectra, LCF data, XRD date, Raman spectra, schematic diagram, ^{1}H NMR spectrum, XAFS measurement, data analysis, computational details, and surface model) is available in the online version of this article at https://doi.org/10.1007/s12274-022-5134-4.

References

[1] Wang, Y. H.; Liu, J. L.; Zheng, G. F. Designing copper-based catalysts for efficient carbon dioxide electroreduction. *Adv. Mater.* **2021**, *33*, 2005798.

[2] Wang, J. J.; Zheng, X. R.; Wang, G. J.; Cao, Y. H.; Ding, W. L.; Zhang, J. F.; Wu, H.; Ding, J.; Hu, H. L.; Han, X. P. et al. Defective bimetallic selenides for selective CO_2 electroreduction to CO. *Adv. Mater.* **2022**, *34*, 2106354.

[3] Sun, X. H.; Tuo, Y. X.; Ye, C. L.; Chen, C.; Lu, Q.; Li, G. N.; Jiang, P.; Chen, S. H.; Zhu, P.; Ma, M. et al. Phosphorus induced electron localization of single iron sites for boosted CO_2 electroreduction reaction. *Angew. Chem., Int. Ed.* **2021**, *60*, 23614–23618.

[4] Gu, J.; Hsu, C. S.; Bai, L. C.; Chen, H. M.; Hu, X. L. Atomically dispersed Fe^{3+} sites catalyze efficient CO_2 electroreduction to CO. *Science* **2019**, *364*, 1091–1094.

[5] Zhang, N. Q.; Zhang, X. X.; Kang, Y. K.; Ye, C. L.; Jin, R.; Yan, H.; Lin, R.; Yang, J. R.; Xu, Q.; Wang, Y. et al. A supported Pd_2 dual-atom site catalyst for efficient electrochemical CO_2 reduction. *Angew. Chem., Int. Ed.* **2021**, *60*, 13388–13393.

[6] Zhang, N. Q.; Zhang, X. X.; Tao, L.; Jiang, P.; Ye, C. L.; Lin, R.; Huang, Z. W.; Li, A.; Pang, D. W.; Yan, H. et al. Silver single-atom catalyst for efficient electrochemical CO_2 reduction synthesized from thermal transformation and surface reconstruction. *Angew. Chem., Int. Ed.* **2021**, *60*, 6170–6176.

[7] Hepburn, C.; Adlen, E.; Beddington, J.; Carter, E. A.; Fuss, S.; Dowell, N. M.; Minx, J. C.; Smith, P.; Williams, C. K. The technological and economic prospects for CO_2 utilization and removal. *Nature* **2019**, *575*, 87–97.

[8] Rodrigues, R. M.; Guan, X.; Iñiguez, J. A.; Estabrook, D. A.; Chapman, J. O.; Huang, S. Y.; Sletten, E. M.; Liu, C. Perfluorocarbon nanoemulsion promotes the delivery of reducing equivalents for electricity-driven microbial CO_2 reduction. *Nat. Catal.* **2019**, *2*, 407–414.

[9] Chen, S. H.; Li, W. H.; Jiang, W. J.; Yang, J. R.; Zhu, J. X.; Wang, L. Q.; Ou, H. H.; Zhuang, Z. C.; Chen, M. Z.; Sun, X. H. et al. MOF encapsulating N-heterocyclic carbene-ligated copper single-atom site catalyst towards efficient methane electrosynthesis. *Angew. Chem., Int. Ed.* **2022**, *61*, e202114450.

[10] De Arquer, F. P. G.; Dinh, C. T.; Ozden, A.; Wicks, J.; McCallum, C.; Kirmani, A. R.; Nam, D. H.; Gabardo, C.; Seifitokaldani, A.; Wang, X. et al. CO_2 electrolysis to multicarbon products at activities greater than 1 $A \cdot cm^{-2}$. *Science* **2020**, *367*, 661–666.

[11] Wang, G.; Chen, Z.; Wang, T.; Wang, D. S.; Mao, J. J. P and Cu dual sites on graphitic carbon nitride for photocatalytic CO_2 reduction to hydrocarbon fuels with high C_2H_6 evolution. *Angew. Chem., Int. Ed.* **2022**, *61*, e202210789.

[12] Jouny, M.; Hutchings, G. S.; Jiao, F. Carbon monoxide electroreduction as an emerging platform for carbon utilization. *Nat. Catal.* **2019**, *2*, 1062–1070.

[13] Zhong, M.; Tran, K.; Min, Y. M.; Wang, C. H.; Wang, Z. Y.; Dinh, C. T.; de Luna, P.; Yu, Z. Q.; Rasouli, A. S.; Brodersen, P. et al. Accelerated discovery of CO_2 electrocatalysts using active machine learning. *Nature* **2020**, *581*, 178–183.

[14] Li, Y.; Shan, W. T.; Zachman, M. J.; Wang, M. Y.; Hwang, S.; Tabassum, H.; Yang, J.; Yang, X. X.; Karakalos, S.; Feng, Z. X. et al. Atomically dispersed dual-metal site catalysts for enhanced CO_2 reduction: Mechanistic insight into active site structures. *Angew. Chem., Int. Ed.* **2022**, *61*, e202205632.

[15] Wang, M. M.; Li, M.; Liu, Y. Q.; Zhang, C.; Pan, Y. Structural regulation of single-atomic site catalysts for enhanced electrocatalytic CO_2 reduction. *Nano Res.* **2022**, *15*, 4925–4941.

[16] Li, R. Z.; Wang, D. S. Understanding the structure-performance relationship of active sites at atomic scale. *Nano Res.* **2022**, *15*, 6888–6923.

[17] Tomboc, G. M.; Choi, S.; Kwon, T.; Hwang, Y. J.; Lee, K. Potential link between Cu surface and selective CO_2 electroreduction: Perspective on future electrocatalyst designs. *Adv. Mater.* **2020**, *32*, 1908398.

[18] Kim, J. Y.; Kim, G.; Won, H.; Gereige, I.; Jung, W. B.; Jung, H. T. Synergistic effect of Cu_2O mesh pattern on high-facet Cu surface for selective CO_2 electroreduction to ethanol. *Adv. Mater.* **2022**, *34*, 2106028.

[19] Arán-Ais, R. M.; Scholten, F.; Kunze, S.; Rizo, R.; Roldan Cuenya, B. The role of *in-situ* generated morphological motifs and Cu(I) species in C_{2+} product selectivity during CO_2 pulsed electroreduction. *Nat. Energy* **2020**, *5*, 317–325.

[20] Zhu, Q. G.; Sun, X. F.; Yang, D. X.; Ma, J.; Kang, X. C.; Zheng, L. R.; Zhang, J.; Wu, Z. H.; Han, B. X. Carbon dioxide electroreduction to C_2 products over copper-cuprous oxide derived from electrosynthesized copper complex. *Nat. Commun.* **2019**, *10*, 3851.

[21] De Luna, P.; Quintero-Bermudez, R.; Dinh, C. T.; Ross, M. B.; Bushuyev, O. S.; Todorović, P.; Regier, T.; Kelley, S. O.; Yang, P. D.; Sargent, E. H. Catalyst electro-redeposition controls morphology and oxidation state for selective carbon dioxide reduction. *Nat. Catal.* **2018**, *1*, 103–110.

[22] Wang, J. L.; Tan, H. Y.; Zhu, Y. P.; Chu, H.; Chen, H. M. Linking the dynamic chemical state of catalysts with the product profile of electrocatalytic CO_2 reduction. *Angew. Chem., Int. Ed.* **2021**, *60*, 17254–17267.

[23] Wakerley, D.; Lamaison, S.; Ozanam, F.; Menguy, N.; Mercier, D.; Marcus, P.; Fontecave, M.; Mougel, V. Bio-inspired hydrophobicity promotes CO_2 reduction on a Cu surface. *Nat. Mater.* **2019**, *18*, 1222–1227.

[24] Wu, Z. Z.; Gao, F. Y.; Gao, M. R. Regulating the oxidation state of nanomaterials for electrocatalytic CO_2 reduction. *Energy Environ. Sci.* **2021**, *14*, 1121–1139.

[25] Liu, J. Z.; Cheng, L.; Wang, Y. T.; Chen, R. Z.; Xiao, C. Q.; Zhou, X. D.; Zhu, Y. H.; Li, Y. H.; Li, C. Z. Dynamic determination of Cu^+ roles for CO_2 reduction on electrochemically stable Cu_2O-based nanocubes. *J. Mater. Chem. A* **2022**, *10*, 8459–8465.

[26] Yang, P. P.; Zhang, X. L.; Gao, F. Y.; Zheng, Y. R.; Niu, Z. Z.; Yu, X. X.; Liu, R.; Wu, Z. Z.; Qin, S.; Chi, L. P. et al. Protecting copper oxidation state via intermediate confinement for selective CO_2 electroreduction to C_{2+} fuels. *J. Am. Chem. Soc.* **2020**, *142*, 6400–6408.

[27] Zang, Y. P.; Liu, T. F.; Wei, P. F.; Li, H. F.; Wang, Q.; Wang, G. X.; Bao, X. H. Selective CO_2 electroreduction to ethanol over a carbon-coated CuO_x catalyst. *Angew. Chem., Int. Ed.* **2022**, *61*, e202209629.

[28] Martić, N.; Reller, C.; Macauley, C.; Löffler, M.; Schmid, B.; Reinisch, D.; Volkova, E.; Maltenberger, A.; Rucki, A.; Mayrhofer, K. J. J. et al. Paramelaconite-enriched copper-based material as an efficient and robust catalyst for electrochemical carbon dioxide reduction. *Adv. Energy Mater.* **2019**, *9*, 1901228.

[29] Wang, R.; Liu, J.; Huang, Q.; Dong, L. Z.; Li, S. L.; Lan, Y. Q. Partial coordination-perturbed Bi-copper sites for selective electroreduction of CO_2 to hydrocarbons. *Angew. Chem., Int. Ed.* **2021**, *60*, 19829–19835.

[30] Li, F. W.; Thevenon, A.; Rosas-Hernández, A.; Wang, Z. Y.; Li, Y. L.; Gabardo, C. M.; Ozden, A.; Dinh, C. T.; Li, J.; Wang, Y. H. et al. Molecular tuning of CO_2-to-ethylene conversion. *Nature* **2020**, *577*, 509–513.

[31] Duan, G. Y.; Li, X. Q.; Ding, G. R.; Han, L. J.; Xu, B. H.; Zhang, S. J. Highly efficient electrocatalytic CO_2 reduction to C_{2+} products on a poly(ionic liquid)-based Cu^0-Cu^I tandem catalyst. *Angew. Chem., Int. Ed.* **2022**, *61*, e202110657.

[32] Li, H. F.; Liu, T. F.; Wei, P. F.; Lin, L.; Gao, D. F.; Wang, G. X.; Bao, X. H. High-rate CO_2 electroreduction to C_{2+} products over a copper-copper iodide catalyst. *Angew. Chem., Int. Ed.* **2021**, *60*, 14329–14333.

[33] Niu, Z. Z.; Gao, F. Y.; Zhang, X. L.; Yang, P. P.; Liu, R.; Chi, L. P.; Wu, Z. Z.; Qin, S.; Yu, X. X.; Gao, M. R. Hierarchical copper with inherent hydrophobicity mitigates electrode flooding for high-rate CO_2 electroreduction to multicarbon products. *J. Am. Chem. Soc.* **2021**, *143*, 8011–8021.

[34] Chen, C. B.; Li, Y. F.; Yu, S.; Louisia, S.; Jin, J. B.; Li, M. F.; Ross, M. B.; Yang, P. D. Cu-Ag tandem catalysts for high-rate CO_2 electrolysis toward multicarbons. *Joule* **2020**, *4*, 1688–1699.

[35] Sun, R. B.; Gao, J. Y.; Wu, G.; Liu, P. G.; Guo, W. X.; Zhou, H.; Ge, J. J.; Hu, Y. M.; Xue, Z. G.; Li, H. et al. Amorphous metal oxide nanosheets featuring reversible structure transformations as sodium-ion battery anodes. *Cell Rep. Phys. Sci.* **2020**, *1*, 100118.

[36] Chu, Y. T.; Guo, L. Y.; Xi, B. J.; Feng, Z. Y.; Wu, F. F.; Lin, Y.; Liu, J. C.; Sun, D.; Feng, J. K.; Qian, Y. T. et al. Embedding $MnO@Mn_3O_4$ nanoparticles in an N-doped-carbon framework derived from Mn-organic clusters for efficient lithium storage. *Adv. Mat.* **2018**, *30*, 1704244.

[37] Chen, K. F.; Lo, S. C.; Chang, L.; Egerton, R.; Kai, J. J.; Lin, J. J.; Chen, F. R. Valence state map of iron oxide thin film obtained from electron spectroscopy imaging series. *Micron* **2007**, *38*, 354–361.

[38] Tahir, D.; Tougaard, S. Electronic and optical properties of Cu, CuO, and Cu_2O studied by electron spectroscopy. *J. Phys. Condens. Matter* **2012**, *24*, 175002.

[39] Pauly, N.; Tougaard, S.; Yubero, F. LMM Auger primary excitation spectra of copper. *Surf. Sci.* **2014**, *630*, 294–299.

[40] Tian, Y. H.; Liu, X. Z.; Xu, L.; Yuan, D.; Dou, Y. H.; Qiu, J. X.; Li, H. N.; Ma, J. M.; Wang, Y.; Su, D. et al. Engineering crystallinity and oxygen vacancies of Co(II) oxide nanosheets for high performance and robust rechargeable Zn-air batteries. *Adv. Funct. Mater.* **2021**, *31*, 2101239.

[41] Velasco-Vélez, J. J.; Jones, T.; Gao, D. F.; Carbonio, E.; Arrigo, R.; Hsu, C. J.; Huang, Y. C.; Dong, C. L.; Chen, J. M.; Lee, J. F. et al. The role of the copper oxidation state in the electrocatalytic reduction of CO_2 into valuable hydrocarbons. *ACS Sustainable Chem. Eng.* **2019**, *7*, 1485–1492.

[42] Wu, G.; Zheng, X. S.; Cui, P. X.; Jiang, H. Y.; Wang, X. Q.; Qu, Y. T.; Chen, W. X.; Lin, Y.; Li, H.; Han, X. et al. A general synthesis approach for amorphous noble metal nanosheets. *Nat. Commun.* **2019**, *10*, 4855.

[43] Gao, J.; Zhang, H.; Guo, X. Y.; Luo, J. S.; Zakeeruddin, S. M.; Ren, D.; Grätzel, M. Selective C–C coupling in carbon dioxide electroreduction via efficient spillover of intermediates as supported by operando Raman spectroscopy. *J. Am. Chem. Soc.* **2019**, *141*, 18704–18714.

[44] Chernyshova, I. V.; Somasundaran, P.; Ponnurangam, S. On the origin of the elusive first intermediate of CO_2 electroreduction. *Proc. Natl. Acad. Sci. USA* **2018**, *115*, E9261–E9270.

[45] Jiang, Y. W.; Wang, X. Y.; Duan, D. L.; He, C. H.; Ma, J.; Zhang, W. Q.; Liu, H. J.; Long, R.; Li, Z. B.; Kong, T. T. et al. Structural reconstruction of Cu_2O superparticles toward electrocatalytic CO_2 reduction with high C_{2+} products selectivity. *Adv. Sci.* **2022**, *9*, 2105292.

[46] Ross, M. B.; Dinh, C. T.; Li, Y. F.; Kim, D.; de Luna, P.; Sargent, E. H.; Yang, P. D. Tunable Cu enrichment enables designer syngas electrosynthesis from CO_2. *J. Am. Chem. Soc.* **2017**, *139*, 9359–9363.

[47] Kim, Y.; Park, S.; Shin, S. J.; Choi, W.; Min, B. K.; Kim, H.; Kim, W.; Hwang, Y. J. Time-resolved observation of C–C coupling intermediates on Cu electrodes for selective electrochemical CO_2 reduction. *Energy Environ. Sci.* **2020**, *13*, 4301–4311.

[48] Mudiyanselage, K.; Kim, H. Y.; Senanayake, S. D.; Baber, A. E.; Liu, P.; Stacchiola, D. Probing adsorption sites for CO on ceria. *Phys. Chem. Chem. Phys.* **2013**, *15*, 15856–15862.

[49] Nitopi, S.; Bertheussen, E.; Scott, S. B.; Liu, X. Y.; Engstfeld, A. K.; Horch, S.; Seger, B.; Stephens, I. E. L.; Chan, K.; Hahn, C. et al. Progress and perspectives of electrochemical CO_2 reduction on copper in aqueous electrolyte. *Chem. Rev.* **2019**, *119*, 7610–7672.

[50] Liu, X. Y.; Xiao, J. P.; Peng, H. J.; Hong, X.; Chan, K. R.; Nørskov, J. K. Understanding trends in electrochemical carbon dioxide reduction rates. *Nat. Commun.* **2017**, *8*, 15438.

[51] Chan, K. R.; Tsai, C.; Hansen, H. A.; Nørskov, J. K. Molybdenum sulfides and selenides as possible electrocatalysts for CO_2 reduction. *ChemCatChem* **2014**, *6*, 1899–1905.

[52] Blyholder, G. Molecular orbital view of chemisorbed carbon monoxide. *J. Phys. Chem.* **1964**, *68*, 2772–2777.